ORIGINAL ARTICLE

lajss.org© Latin American Journal of Solids and Structures

www.lajss.org

High-hardness polyurea coated steel plates subjected to combined loadings of shock wave and fragments

Long Zhang[a], Xin Wang[a], Yuting Wang[a], Juan Gu[b], Chong Ji[a*], Gang Wu[a], Liangyu Cheng[c]

[a] College of Field Engineering, Army Engineering University of PLA, Nanjing 210007, China. E-mails: 842689805@qq.com; 310433804@qq.com; wangyuting@njust.edu.cn; 2468645816@qq.com; 1392520073@qq.com

[b] College of National Defense Engineering, Army Engineering University of PLA, Nanjing 210007, China. E-mails: gujuan0617@126.com

[c] Army Academy of Artillery and Air Offense of PLA Nanjing Campus, Nanjing 211131, China. E-mails: clychmy@qq.com

* Corresponding author.

https://doi.org/10.1590/1679-78256882

Abstract

To investigate the effect of polyurea on the protective performance of a steel target plate under the combination of shock wave and fragments, the failure characteristics, damage process and micro mechanism of the polyurea coated steel plates with different coating methods under the combination of explosion shock waves and fragments were analyzed through experiments and numerical simulations. The results showed that single-sided coatings aggravated the damage of target plate when the coating thickness was 2 mm. While the polyurea thickness greater than 4 mm could significantly reduce the damage degree of the steel plate. When the polyurea was coated on the double sides, it would aggravate the damage, no matter how thick the polyurea was. Through microscopic research, it was found that the front coated polyurea was severely ablated by detonation products, which greatly reduce its energy absorption efficiency. The polyurea coated on the back underwent tensile fracture under the influence of tensile stress wave. The breaking of intramolecular hydrogen bond of polyurea was the key to the energy absorption of polyurea.

Keywords

Blast shock wave; Fragments; Combined effect; Polyurea; Numerical simulation; ASTM1045 steel

Graphical Abstract

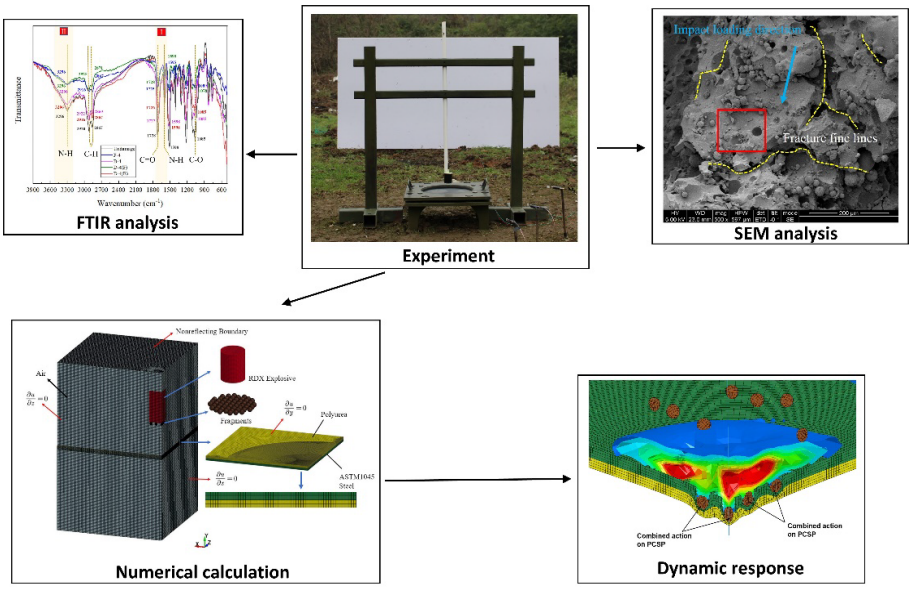

Received November 21, 2021. In revised form February 02, 2022. Accepted February 02, 2022. Available online February 02, 2022
https://doi.org/10.1590/1679-78256882

1 INTRODUCTION

Polyurea (PU) is a high-molecular-weight material mainly produced by the reaction of isocyanate and amino compounds. PU has very significantly nonlinear mechanical characteristics, a strong strain rate correlation, a high elastic modulus (Wang et al., 2019). When it is impacted or penetrated, PU can absorb a significant amount of energy and shows excellent explosion and penetration resistance due to its glass transition, its connection with the substrate, and the damage of the adhesive layer (Toutanji et al., 2013).

In general, improving the anti-penetration and anti-blast performances of steel structure can be achieved by increasing the thickness of the steel. However, due to the limitations of weight and volume, the above methods cannot produce the best effect (Crouch, 2019). In recent years, improving the performances of matrix materials by film technology, surface modification technology, and coating technology has become a popular research area in the industry. In particular, PU coating spraying technology is used to improve the blast and penetration resistances of metallic or nonmetallic materials, and the performance is particularly outstanding (Stergiou et al., 2021; Grujicic et al.,2012).

In recent years, with the increasing uncertainty in the world, the risk level of threats such as terrorist attacks and local wars has further increased, which creates higher requirements for the anti-explosion and anti-penetration abilities of machinery, buildings, weapons, and equipment based on steel. The high-speed impact energy absorption of a material is the key factor that determines its explosion and penetration resistance. Due to the constraints of the material's hardness, toughness, tensile strength, and yield strength, the explosion and penetration resistances of steel are limited (Jacobs and Van Dingenen, 2001; Jena et al., 2010). Many scholars have found that PU can significantly enhance the explosion resistance (Ackland et al., 2013; Nemat-Nasser, 2010; Amini et al., 2010; Zeng et al., 2021) or anti-penetration performances (Mohotti et al., 2015, 2014; Huang et al., 2018) of metal structures. Dinesh et al. (2021) conducted numerical simulations to study the anti-explosion performances of PU-reinforced steel plates with different coating methods and different coating thicknesses under the impact of different equivalent trinitrotoluene (TNT) explosives. Wu et al. (2021a) compared the damage effects on aluminum alloy circular pipes with different PU coating methods under explosion loads through experiments and numerical simulations and found that the damage degree of the aluminum alloy pipe under impact loads can be reduced by coating with PU. Dewapriya and Miller (2021) demonstrated the penetration resistance of nano-PU-layer-reinforced aluminum foil films through molecular dynamics simulations. It was found that a PU coating on the front of an aluminum film could effectively reduce the damage caused by nano-bullet penetration, while the reflection of the PU coating on the back weakened the anti-penetration performance of the aluminum foil film. Sun et al. (2021) compared the residual velocity of projectile and failure modes of composite target plates with different coating methods, thicknesses, and types of PU subjected to projectile penetration. It was found that the penetration resistance of the PU-coated target plate was enhanced and the resistance effect varied with the type of PU.

Damages from various types of ammunition or improvised explosive devices (IEDs), which are common in military operations and terrorist attacks, involve the dual role of explosion shock waves and fragments. Under the combined action of an explosion shock wave and fragments (hereinafter referred to as 'combined action'), once the relevant protective structure is broken, the shock and fragments will pose a great threat to the structure, internal equipment, and personnel (Chepkenen et al., 2020). A large number of studies have shown that the failure mode of a metal structure under combined action is more complex and variable under the action of a single factor and will produce more significant damage (Kong et al., 2014; Nyström and Gylltoft, 2009; Duan et al., 2015; Leppaenen, 2005). At present, most of the research has focused on the single-factor anti-explosion or anti-penetration performances of PU-coated structures, but less research on the combined action of blast shock waves and fragments has been reported. In reality, all kinds of weapons, equipment, and engineering buildings cannot be effected only by a single factor when they are attacked. Therefore, it is crucial to enhance the anti-blast and anti-penetration effects of engineering structures.

It is not difficult to find that most of the materials used in the study on the resistance of polyurea composite structures to strong impact load were limited to "soft" polyurea elastomers. Compared with this, the failure characteristics of high hardness polyurea materials to impact load (especially under the combined action of multiple loads) were not clear, and the relevant studies had not been reported.

The damage to a structure caused by explosion shock waves and fragments occurs in a very short time. It is often impossible to generate combined action consistently while also obtaining detailed data. Numerical simulations can make up for the shortcomings of experiments to obtain detailed and comprehensive data and results (Molnar et al., 2015). In this study, to improve the explosion and penetration resistance of existing structures, PU-coated ASTM1045 steel plates (hereinafter referred to as 'PCSPs') were selected as the research object. Numerical simulations supplemented by experimental verification were used to study the deformation, dynamic response characteristics, impulse change process and energy absorption characteristics of PCSPs. Furthermore, the damage and energy absorption mechanism of PCSP were discussed by SEM and FTIR.

2 EXPERIMENTAL AND NUMERICAL SIMULATION METHODS

In this paper, numerical simulations were used to study the damage mechanism and protective performance behaviors for PCSPs under the combined effect of shock wave and fragments. Therefore, an appropriate and reasonable numerical simulation method is important. Relevant experiments are essential to verify the accuracy of the numerical simulation results.

2.1 Target plate processing and experiment setup

2.1.1 Characteristics of target plates

The manufacturing of the PCSPs was conducted in strict accordance with steps I–III shown in Figure 1. AMMT-53 PU was selected as the coating layer, and ASTM1045 steel was adopted as the substrate, with a size of 400 mm × 400 mm × 4 mm. The bonding strength of a specific binder was about 2 MPa.

In our previous research, mechanical tests had been carried out to study the dynamic performance of the PU under different strain rates, and the relevant parameters had been obtained (Wu et al., 2021b). The results showed that the PU has low tensile strength and elongation, and exhibits obvious strain rate sensitivity at high strain rates. Table 1 shows the parameters of the AMMT-53 PU. In general, AMMT-53 PU is mainly characterized by low elongation at break and high surface hardness. Based on its mechanical properties, it can be called as “high hardness” PU, which is mostly referred to as PU in the follow-up content. Table 2 shows the specific spraying scheme. In Table 2, the configurations are labeled S/F/B/D-X, where X indicates the thickness of the PU coating, and S, F, B, and D indicate that there was no coating and that the coating was on the front, back, and double faces of the steel plate, respectively.

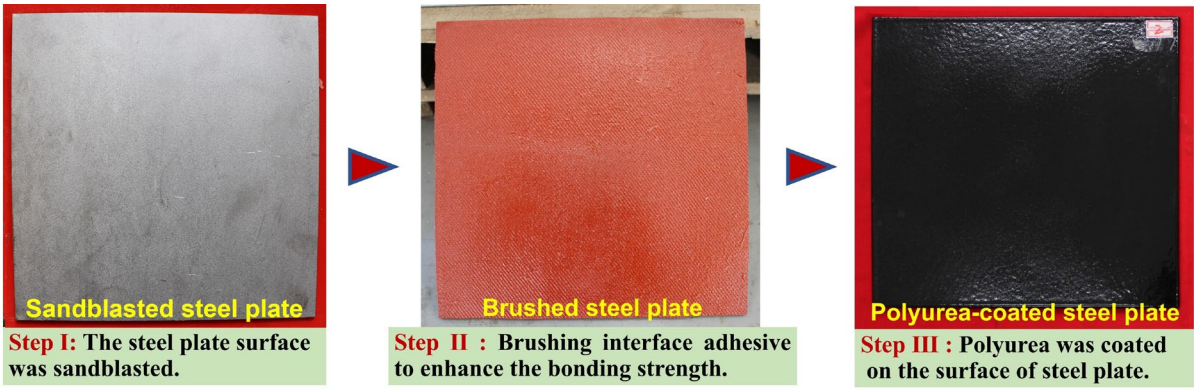

Figure 1 Manufacturing process of the PCSPs.

Table 1 Parameters of the AMMT-53 PU.

Solid content/%	Gelation time/s	Tensile strength/MPa	Elongation at break/%	Tear strength/(kN/m^{-1})	Hardness /HD	Shock resistance /(kg·m)
98	20	25	50	90	70	1.5

Table 2 Specific scheme of spraying.

Number	Condition number	Thickness of steel/mm	Thickness of PU/mm	Coating position
1	S-0	4	0(No coating)	No coating
2	F-2	4	2(Front face)	Front
3	F-4	4	4(Front face)	Front
4	F-6	4	6(Front face)	Front
5	B-2	4	2(Back face)	Back
6	B-4	4	4(Back face)	Back
7	B-6	4	6(Back face)	Back
8	D-2	4	2(Front face) +2(Back face)	Double-sided
9	D-4	4	4(Front face) +4(Back face)	Double-sided
10	D-6	4	6(Front face) +6(Back face)	Double-sided

2.1.2 Experiment setup

To study the resistance of the PCSP to the combined action, the test device shown in Figure 2 was designed. The area of the target plate beyond 320 mm from the center diameter of the steel plate was fixed with steel clamps. The combined action was realized by using a prefabricated fragment explosive. The explosive was a 150 g cylindrical Herzog (RDX) with a height of 56 mm and a bottom diameter of 48 mm, and 55 tungsten steel balls with diameters of 5 mm were pasted evenly on the bottom surface of the explosive to represent the prefabricated fragments. The bottom end of the explosive was 60 mm high in the axial direction of the center of the target plate.

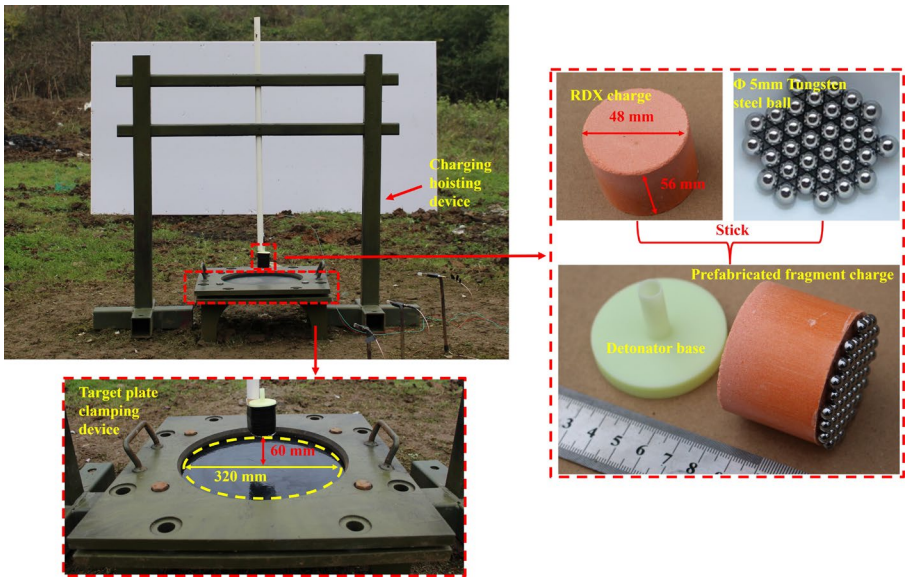

Figure 2 Experiment setup.

2.2 Establishment of numerical simulation model

To establish a numerical simulation model corresponding to the experiments, the test device can be simplified to the physical model shown in Figure 3.

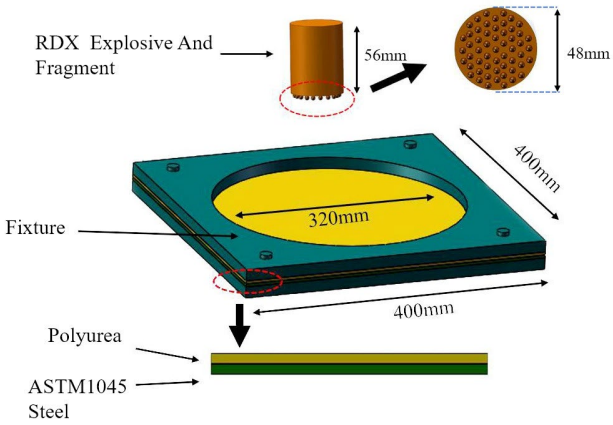

Figure 3 Physical model diagram.

The ANSYS/LS-DYNA nonlinear-dynamics finite element analysis software was used to model the combined action on the PCSPs. As shown in Figure 4, a 1/4-model was established based on the principle of symmetry. SOLID164 is the element type by the solid components in this manuscript. However, different algorithms were adopted for different components. Fragments, steel plate and PU layer were constructed by Lagrangian algorithms to accurately describe the deformation and failure characteristics, in which the material was attached to the element and moved or deformed with the element. The lagrangian algorithm can also describe the motion of structure boundary very accurately. RDX Explosive and air were based on the ALE (Arbitrary Lagrangian Eulerian) algorithm. The spatial grid can move arbitrarily in this

algorithm. As for ALE algorithm, one or several Lagrange time step calculations are performed first, in which the cell mesh is deformed with the flow of materials, and then ALE time step calculations are performed.

Through trial simulations, it was determined that the effect of applying a Y-directional constraint to the area beyond 320 mm from the center diameter of the target plate was almost the same as the effect of clamping, and the solution time could be greatly reduced. Therefore, a Y-directional constraint was applied to simulate the fixing effect of the clamp on the target plate. the damage model is sensitive to the element size, especially for elements through the thickness. When the local strain is too large in a nonlinear analysis process and the elements are seriously distorted, it may lead to inaccurate calculation results or even calculation interruption due to error. To improve the accuracy of simulation, the elements must be fine enough. But at the same time, it will cause a significantly increasing in calculation time. This requires a trade-off between these two, choosing the appropriate element density as much as possible, and taking into account the calculation efficiency while ensuring the calculation accuracy. Therefore, considering the accuracy of simulation and calculation efficiency, the elements of steel plate and PU in the center damaged area of the target plate (the circular area with the center of the target plate and radius of 80 mm) was set as 1.5mm in the length direction, the element through-the-thickness was set as 1.0mm, that is, the steel plate was divided into 4 elements in the thick direction, and the other areas were set as dense to sparse gradient mesh. The element number of PU was different due to the different coating thickness of each working condition. The element size of fragments was 1.0mm, and that of air and explosives was 2.0mm. In the calculation model, the number of elements of steel plate, fragments, explosives and air was 23408, 3520, 1012 and 448437 respectively.

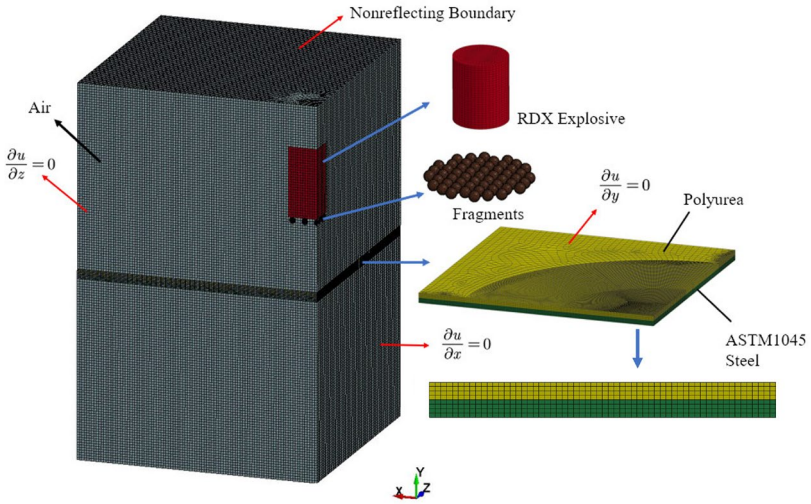

Figure 4 Finite element numerical simulation model.

To simulate the fluid-solid coupling effect, the arbitrary Lagrangian-Eulerian (ALE) algorithm was used for the explosive and air, and the Lagrangian algorithm was used for the fragments, steel plate, and PU. The bond effect between the steel plate and the PU layer was defined by the keyword *CONTACT_A-UTOMATIC_SURFACE_TO_SUR-FACE_TIEBREAK. When the stress on the interface was greater than the set value, the two materials would undergo degumming delamination. The keyword *CONTACT_ERODING_SURFACE_TO_SURFACE was used to define the penetration effect of the fragments on the steel plate and PU components.

2.3 Material models

2.3.1 RDX charge

The *MAT_HIGH_EXPLOSIVE_BURN and Jones–Wilkins–Lee (JWL) equation of state were used to describe the explosion effect of the passivated RDX. The JWL equation is as follows:

$$P_{cj}=A_1\left(1-\frac{\omega}{R_1V}\right)e^{-R_1V}+B_1\left(1-\frac{\omega}{R_2V}\right)e^{-R_2V}+\frac{\omega e_0}{V} \tag{1}$$

where ρ is the density of the RDX, P_{cj} is the detonation pressure, $A_1$and B_1 are calculation constants, R_1, R_2, and ω are fitting parameters, and V is the relative volume. The relevant data are shown in Table 3 (Xu et al., 2008).

Table 3 Parameters for RDX model.

ρ/(kg·m^{-3})	D/(m·s^{-1})	P_{cj}/GPa	A_1/GPa	B_1/GPa	R_1	R_2
1600.0	7910.0	26.5	573.2	14.64	4.6	1.4

2.3.2 Air

The *MAT_NULL material model and the EOS_LINEAR_POLYNOMIAL equation of state were selected to describe the air. The linear polynomial equation of state is as follows:

$$P = C_0 + C_1\mu + C_2\mu^2 + C_3\mu^3 + \left(C_4 + C_5\mu + C_6\mu^2\right)e_0 \tag{2}$$

where C_0–C_6 are coefficients of the equation, and e_0 is the internal energy of air in the ideal state. The relevant parameters are shown in Table 4 (Wu et al., 2021b).

Table 4 Related parameters of air model.

C_0	C_1	C_2	C_3	C_4	C_5	C_6
0	0	0	0	0.4	0.4	0

2.3.3 ASTM1045 steel

The *MAT_PLASTIC_KINEMATIC constitutive model was used to describe the dynamic mechanical behavior of the ASTM1045 steel material. The high-strain-rate effect of the model can be described by the Cowper–Symonds model equation:

$$DIF = 1 + \left(\frac{\dot{\varepsilon}}{C}\right)^{\frac{1}{P}} \tag{3}$$

The yield stress is represented by the amplification factor, which is related to the strain rate. When the stress is greater than the coefficient, the failure effect begins to appear. The equation of yield stress is as follows:

$$\sigma_Y = \left[1 + \left(\frac{\dot{\varepsilon}}{C}\right)^{1/p}\right]\left(\sigma_0 + \beta E_p \varepsilon_p^{eff}\right) \tag{4}$$

where $\dot{\varepsilon}$ is the strain rate, σ_0 is the static yield strength, C and P are Cowper–Symonds strain rate parameters, and E_p represents the strain hardening index. The relevant parameters are shown in Table 5 (Nan et al., 2013).

Table 5 Parameters of ASTM1045 steel model.

ρ/(kg·m^{-3})	E/GPa	M	σ_0/GPa	E_p/GPa	C/s^{-1}
7830.0	210.0	0.30	0.355	10.0	1.0

2.3.4 Tungsten alloy fragments

To describe the penetration behavior of the tungsten alloy fragments into the target plate, the *MAT_JOHNSON_COOK constitutive model combined with the Mie–Grüneisen equation of state was selected. The flow stress expression of the Johnson-Cook model is as follows (Johnson and Cook, 1983):

$$\sigma_y = (A + B\overline{\varepsilon}^{pn})(1 + C\ln\dot{\varepsilon}^*)(1 - T^{*m}) \tag{5}$$

where $\overline{\varepsilon}^p$ is the equivalent plastic strain, $\dot{\varepsilon}^*$ is the dimensionless plastic ratio, T^* is the relative temperature, A represents the yield stress, B represents the strain-hardening coefficient, n is the strain hardening index, C is the strain rate correlation coefficient, and m is the temperature correlation coefficient. The relevant parameters are shown in Table 6 (Lundberg et al., 2006).

Table 6 Parameters of tungsten alloy model.

ρ/(kg·m^{-3})	*A*/MPa	*B*/MPa	*C*	*m*	*n*
17600.0	1410.0	220.0	0.022	1.00	0.11

2.3.5 PU

Due to the significant strain rate effect of PU material under an impact load, the following conditions should be satisfied when selecting its material model (Wang, 2017): (1) the fracture yield criterion of PU elastomer can be simulated, (2) the deformation process of the elastic and plastic sections of the PU can be simulated, and (3) the strain-rate effect of PU under the action of penetration can be simulated.

The *MAT_PIECEWISE_LINEAR_PLATICITY multi-linear elastoplastic material model can satisfy the above conditions, and the PU strain characteristic curve can be combined with this material model to further improve its reliability. The material model needed to input physical parameters, true stress-effective plastic strain curve and strain rate-DIF_1 (dynamic growth factor) curve to complete the definition of polyurea material (Raman et al., 2012; Shi et al., 2019). To better describe polyurea materials in numerical calculations the accuracy of the model was optimized and improved by using the static and dynamic mechanical properties of the polyurea obtained by mechanical tests (Wu et al., 2021b). When defining the curves, the conversion from engineering stress σ_E to true stress σ_T and from engineering strain ε_E to true strain ε_T can be realized by the following formula:

$$\sigma_T=\sigma_E(1+\varepsilon_E) \tag{6}$$

The effective plastic strain εeff was calculated by the following formula:

$$\varepsilon_T=\ln(1+\varepsilon_E) \tag{7}$$

The strain rate characteristics of polyurea were described by the following formula (Raman et al., 2013):

$$DIF_1=a\ln(\dot{\varepsilon})+b \tag{8}$$

$$\sigma_y=\sigma_1 \bullet DIF_1 \tag{9}$$

Where σ_y is the yield strength of polyurea at different strain rates; σ_1 is the yield strength of polyurea under quasi-static conditions; *a* and *b* are the curve fitting factor. The relevant parameters are shown in Table 7.

Table 7 Parameters of PU.

ρ/(kg·m^{-3})	*E*/GPa	*PR*	*SIGY*/GPa	*ETAN*	*FAIL*	*TDEL*
1020.0	0.0019	0.3	1.73E-04	0	0.65	0

3 FAILURE MODES OF PCSPS AND DAMAGE CHARACTERISTICS

3.1 Macro failure model

Figure 5 shows the results of the experiments and numerical simulations. The results showed that regardless of the structure adopted, the damage in the central area of the target plate was the most significant. The failure modes of each target plate are summarized as follows:

Mode I: Large inelastic deformation. Except for large-deflection deformation, no other damage occurred.

Mode II: Plugging failure. The center of the target plate was sheared under the load, and a break hole occurred.

Mode III: Tear failure. Strip tear marks or tear holes appeared on the target plate.

Mode IV: Petalling failure. The central area of the target plate was completely destroyed, forming a 'petal' structure and bending backward.

The damage degree of the various failure modes increased from Mode I to Mode IV.

To verify the correctness of the numerical simulation results, the failure modes and the maximum deformation (δ) values of the target plate were selected as the indices for comparison, as shown in Figure 5. An example of δ is shown in

Figure 6. Figure 7 shows the overall failure modes of the target plates under various working conditions. It can be concluded that the results of the numerical simulation were basically consistent with the experiment results, and the error was within an allowable range. Therefore, the simulation model and material parameters were reliable and could be used for subsequent analysis and simulations.

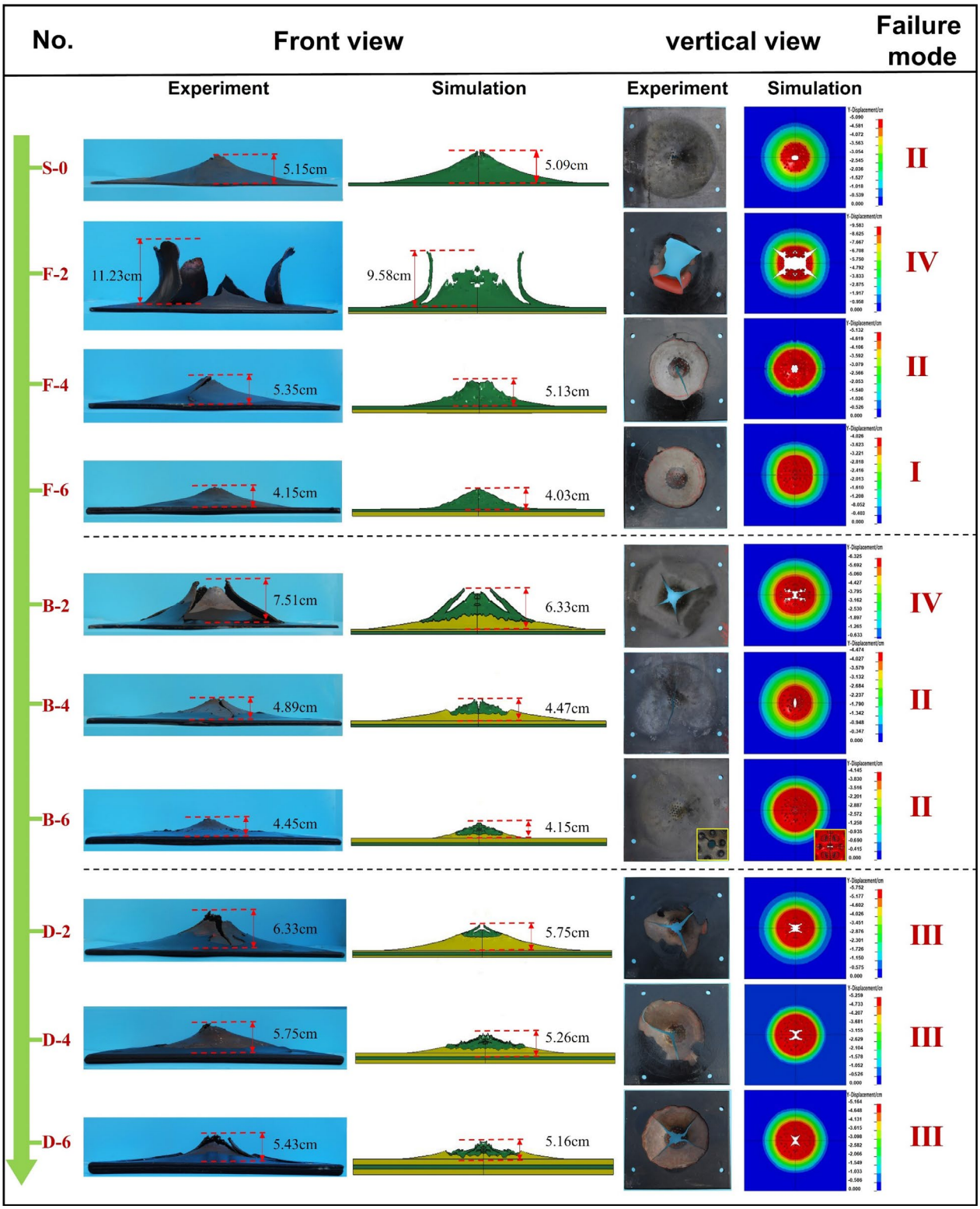

Figure 5 Experimental and simulation results.

(a) Experiment results (b) Simulation results

Figure 6 Maximum deformation (δ) in experiments and simulations.

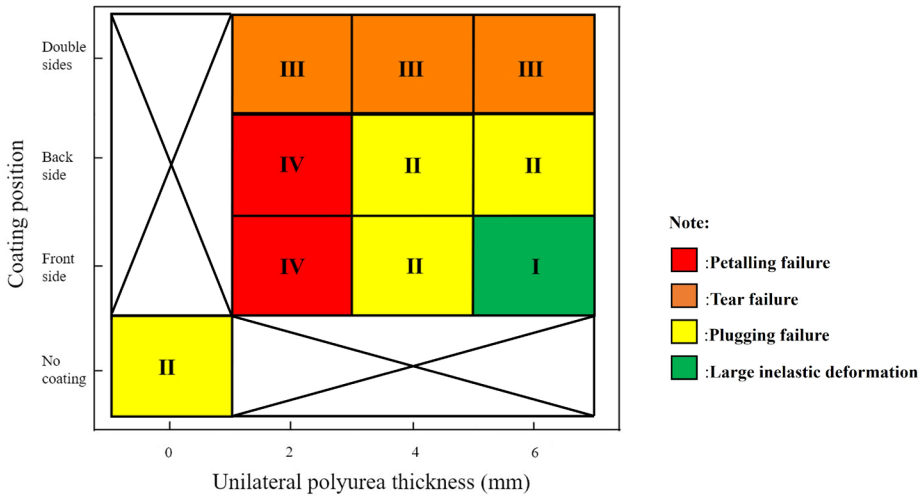

Figure 7 Failure modes of the target plates under various conditions.

The simulation results showed that F-2 and B-2 engendered petalling failure and produced four 'petals' after being subjected to combined loading. S-0, F-4, B-4, and B-6 underwent plugging failure, and fracture fragments were observed. The sizes of the plugging holes for S-0, F-4, B-4, and B-6 were 3.02 cm × 2.26 cm, 3.18 cm × 4.96 cm, 1.26 cm × 3.42 cm, and 0.52 cm × 0.52 cm, respectively. D-2, D-4, and D-6 showed tearing failure. A break hole formed at the center of each of these plates, and four cracks extended from the broken hole. The lengths of the longest crack in these plates were 5.34, 4.06, and 3.46 cm, respectively. F-6 showed the least damage, and only deflection deformation occurred.

The steel plate central unit of each target plate was selected as the research object. The order of the maximum deformation (δ) values of each steel plate from the simulations was F-2 > B-2 > D-2 > D-4 > D-6 > F-4 > S-0 > B-4 > B-6 > F-6. In this order, the calculated maximum deformation values of each PCSP were 188.2%, 124.4%, 113.0%, 103.3%, 101.4%, 100.8%, 87.8%, 81.5%, and 79.2% of the deformation of S-0, respectively. Figure 8 shows the comparison of the maximum deformation (δ) values and the failure modes of the PCSPs with different coating structures.

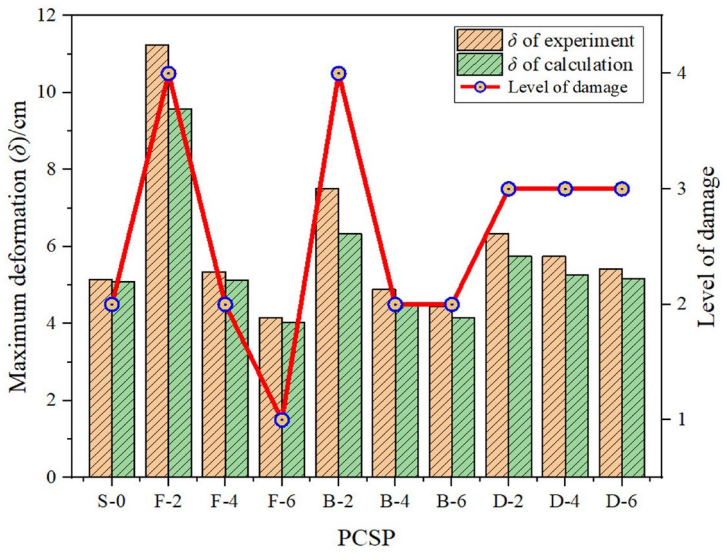

Figure 8 Maximum deformation (δ) values and level of damage of PCSPs with different coating structures.

Based on the failure modes and the maximum deformation (δ) values of the target plates, it was concluded that when PU with a thickness of less than 4 mm was coated on a single side, the damage of the target plate was greatly exacerbated, showing the petalling failure mode. When the thickness of the PU was greater than or equal to 4 mm, the damage degree of the target plate would be reduced with the increase in the PU thickness, and the effect of the front coating was better than that of the back coating. When both sides were coated with PU, the damage degree of the target plate was aggravated, regardless of the thickness.

3.2 Micro damage mechanism

To further study the damage mechanism of PU with different coating modes under the combined action, the fracture edges of undamaged PU and damaged PU of the above three working conditions (F-4, B-4 and D-4) were sampled, scanned and analyzed by SEM.

Figure 9 shows the SEM results of undamaged PU samples. It can be seen that there were a large number of pores on the surface, showing the characteristics of loose and porous "cheese-like" structure, which was the inevitable result of the processing technology that PCSP used compressed air to spray PU on the surface of steel plate through a special spray gun. The loose and porous structure was not only conducive to the rapid solidification of PU, but also the absorption of energy under high-speed load.

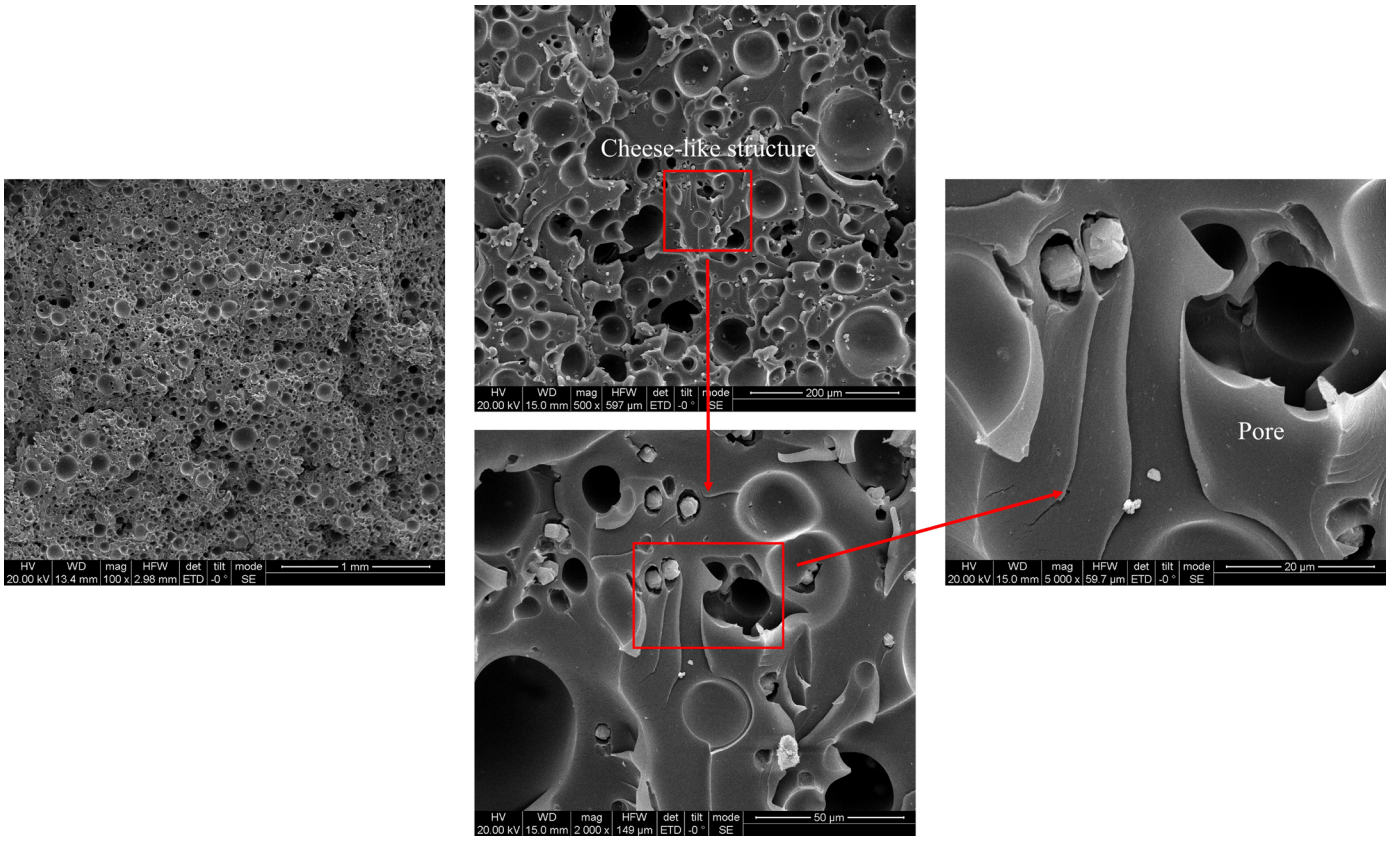

Figure 9 The microstructure of undamaged PU.

Figure 10 shows the scanning results of PU (fragments) from the central failure area of F-4. It can be seen that the whole PU surface was smoother and denser than original material, due to the direct damage by the combined action and ablation by detonation products. When enlarged, it could be observed that the original pores were covered by the condensed PU after ablation. At the same time, only large cracks can be observed in this area, and the cracks had been filled with condensed PU, so the detailed characteristics of PU fracture could not be seen. However, it could be inferred that the long-range molecular chain of PU had been damaged and cannot play the role of energy absorption again. Therefore, when PU was coated on the front face, the ablation effect of detonation products on PU could not be ignored.

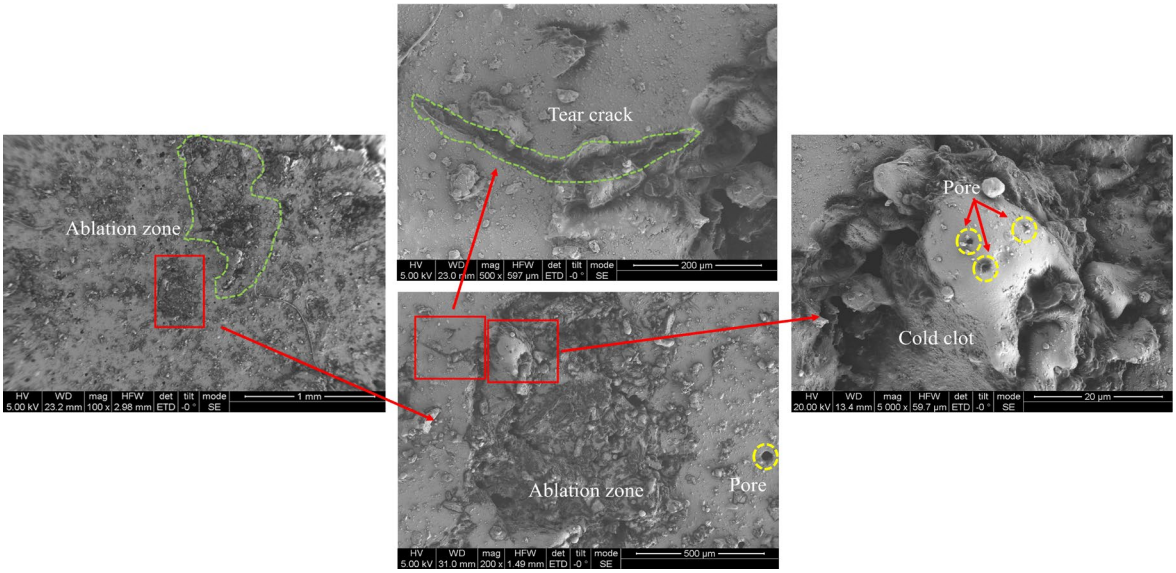

Figure 10 The microstructure of PU in condition F-4.

Figure 11 shows the scanning results of PU (fragments) from the central failure area of B-4. The failure characteristics of PU coated on the back were significantly different from those coated on the front. It could be observed that serious tear failure occurred on the surface of PU, showing the characteristics of tensile fracture even forming deep fracture gullies. After enlarging the fracture gullies, more subtle tear lines and spallation bands along the impact loading direction can be observed. This was due to the ductile fracture caused by the propagation of tensile stress wave between layers, forming fine fracture lines in the fault zone, gradually accumulating and finally producing large-scale fracture. This phenomenon shows that the damage effect of PU was mainly caused by tensile stress. When damaged by combined action, the tensile stress in the PU coated on back exceeded the maximum tensile stress, resulting in PU fracture. After magnification to 100 μm, the fractured pores and fragments in the pores could be observed. It was worth noting that a large number of spherical condensing structures could be observed in the scanned images. This was because the PU on the back face was not directly affected by the detonation products, but after the steel plate was broken, the remaining detonation products would also ablate the PU, but the ablation effect was weak. The PU at the fracture would only melt on a small scale to form small droplets, and then condense and solidify to form a spherical condensation structure.

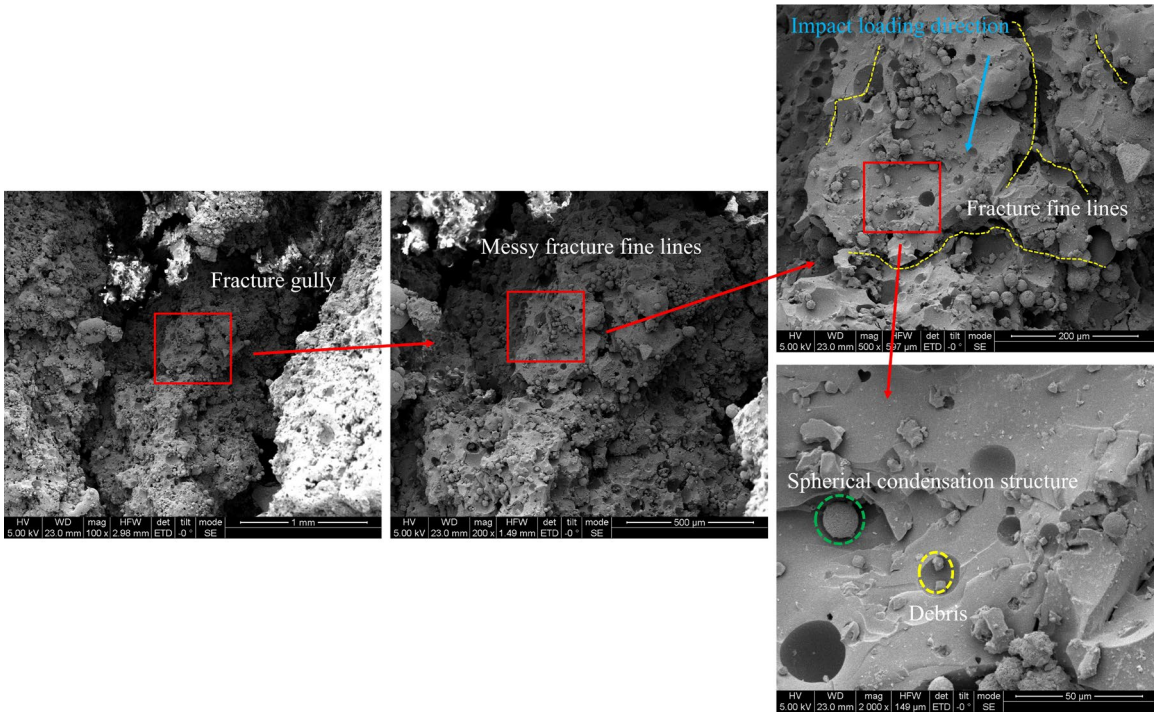

Figure 11 The microstructure of B-4 PU. Debris.

Figure 12 shows the scanning results of PU in the central damaged area of the front and rear plates of D-4. In general, the micro failure characteristics of the PU coated on front were similar to those of F-4. Similarly, the condensed products after ablation by detonation products can be observed in a large area, and obvious ablation traces can be observed after amplification. The failure characteristics of PU coated on the back were also similar to that of B-4, with large-scale tensile fracture, and the spallation crack produced by PU under tensile stress can be obviously observed.

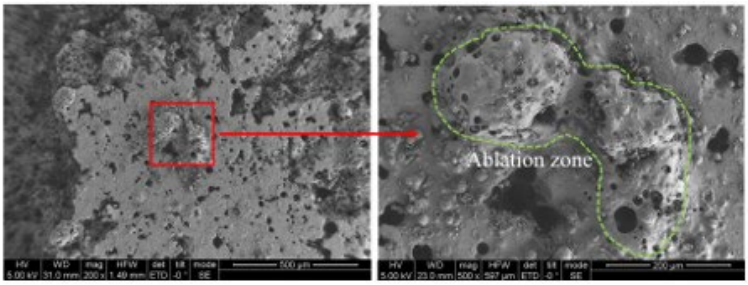

(a) The PU on front face.

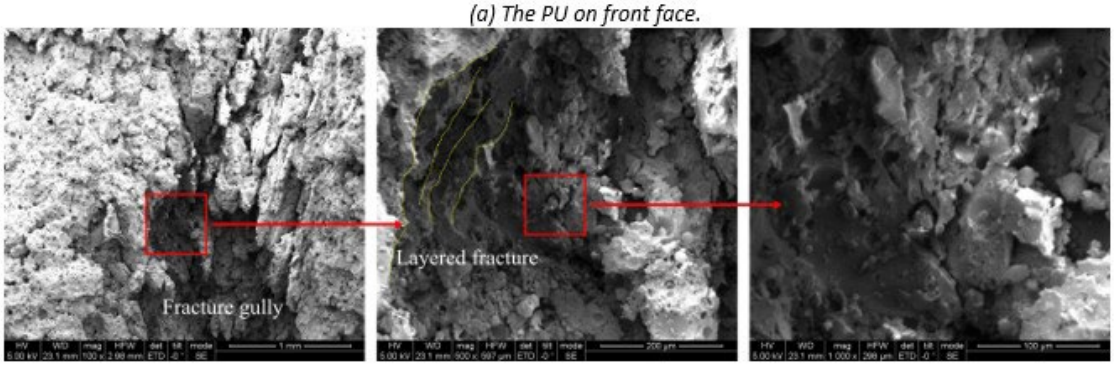

(b) The PU on back face.

Figure 12 The microstructure of D-4 PU.

4 DYNAMIC RESPONSE PROCESSES OF PCSPS

The damage process of PCSPs under the combined action was an instantaneous process that occurred in a very short time, both macro and micro research only reflect the results. To understand the mechanism, it is necessary to analyze it from the dynamic process. The ANSYS/LS-DYNA finite element analysis software could reliably simulate the dynamic responses of the coated plates to the combined action. The dynamic images and relevant simulation data obtained in this process can provide reliable support for further analysis.

4.1 Detonation wave propagation and fragment dispersion

In this study, RDX was detonated by upper-end center initiation. After initiation, the detonation wave propagated downward as a spherical wave, as shown in Figure 13. In the process of propagation, the detonation front expanded gradually. When t = 4.8 μs, the detonation wave reached the bottom of the charge. It was then compressed into a plane wave basically and transformed into a shock wave. The fragments at the bottom of the explosive began to fly outward under the action of a shock wave.

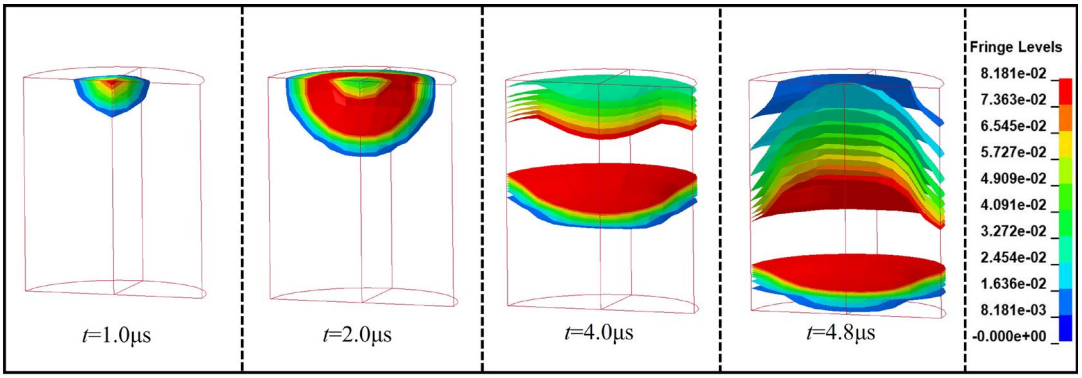

Figure 13 Propagation of detonation wave in RDX

The scattering process of the fragments is shown in Figure 14. The shock wave formed by the explosion had the maximum pressure at the center and gradually decreased in the surrounding area. Therefore, the fragment at the center obtained the maximum velocity. The velocities of the fragments in the surrounding area gradually decreased along the vertical direction. However, the velocity component in the horizontal direction was obtained.

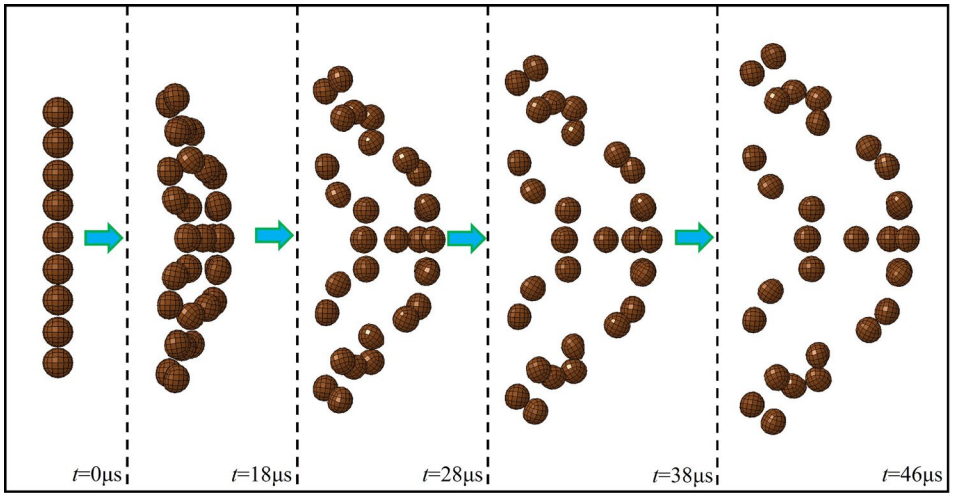

Figure 14 Process of fragment movement.

As shown in Figure 15, when t = 28 μs, the shock wave reached the target plate before the fragments, and the target plate was only subjected to a shock wave. At t = 48 μs, the fragment at the center hit the target plate. After 48 μs, the target plate was subjected to combined action.

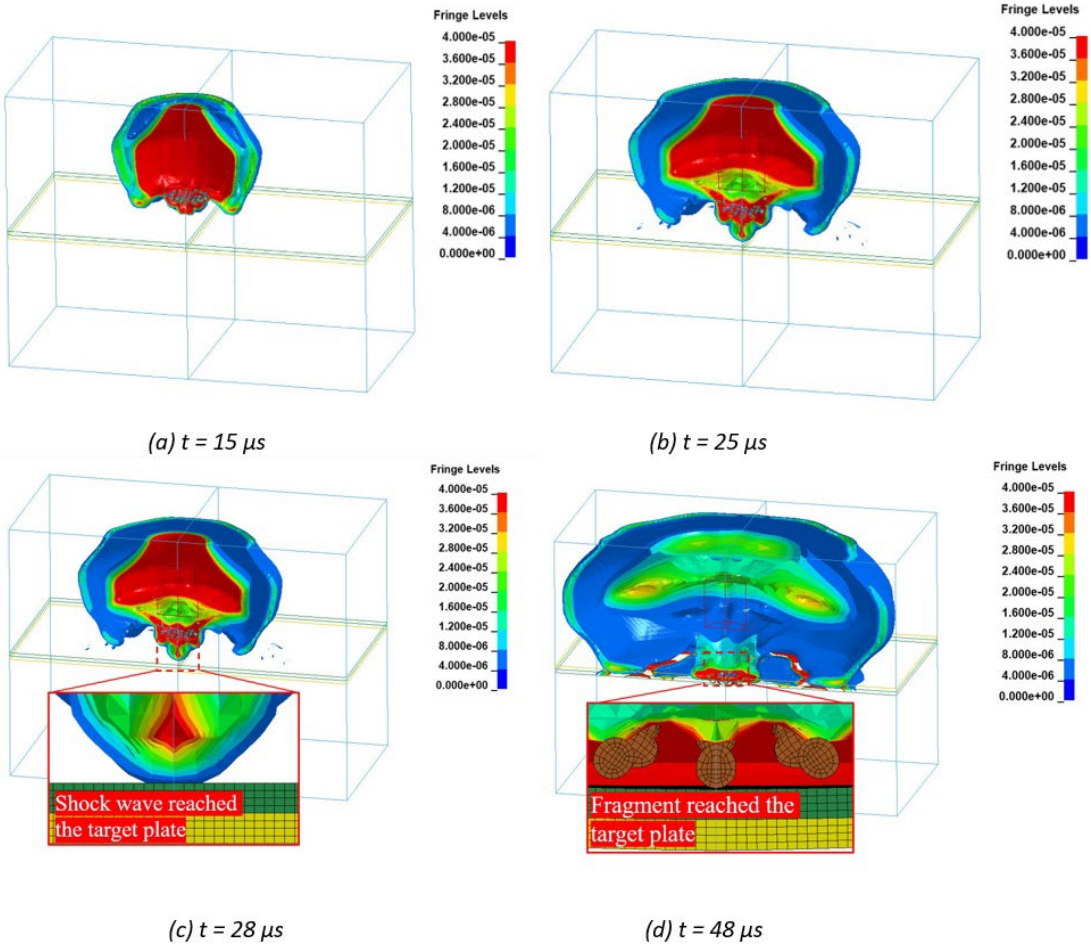

(a) t = 15 μs *(b) t = 25 μs*

(c) t = 28 μs *(d) t = 48 μs*

Figure 15 Sequence of shock wave and fragments impacting the steel plate.

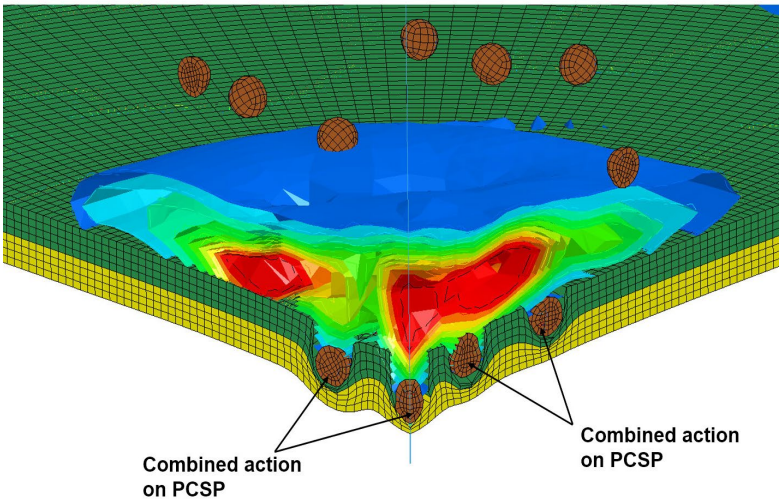

Figure 16 Combined action of shock wave and fragments on target plate.

Part of the energy generated by the charge explosion was used to drive the fragments, and the energy of the shock wave acting on the target was lower than that of the equivalent charge without fragments. However, due to the presence of the fragments, turbulence was generated in the shock wave from the edges of the fragments to the geometric center of the fragment, which combined and superimposed with the shock wave in front of the fragment to form a high-pressure area with a stronger pressure. As a result, the target plate was impacted more violently (Zheng et al., 2019). The combined action on the target plate is shown in Figure 16. Therefore, the combined action of the shock wave and the fragments was not just a simple superposition.

4.2 Dynamic response process of PCSP

To reveal the protection mechanism of the PCSP, the response process of the PCSP under the combined action was analyzed.

4.2.1 Dynamic response of uncoated PU target plates

Figure 17 shows that the failure process of S-0 was due to the combined action, and S-0 showed plugging failure damage characteristics. The specific failure process is as follows:

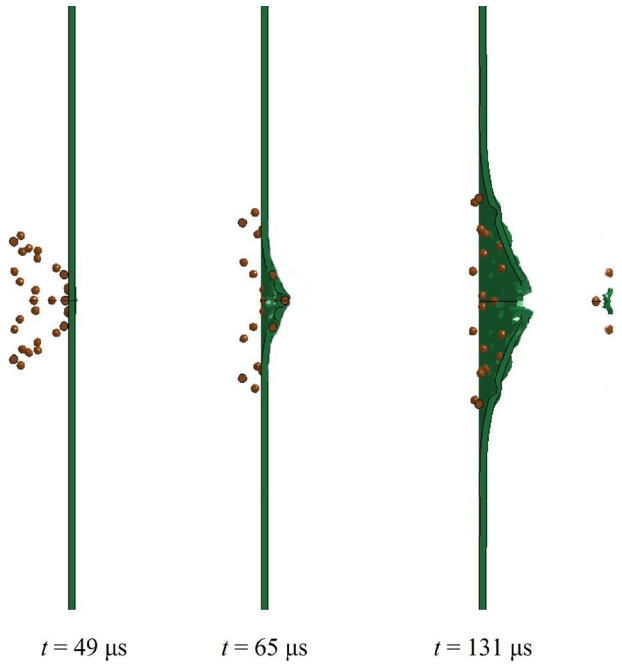

Figure 17 Process of shock-fragments loading on the target plate of group S-0.

Stage 1. The shock wave reached the target plate before the fragments, and the target plate began to deform under the action of the shock wave.

Stage 2. With the arrival of the fragments, they superimposed with the shock wave pressure and produced a huge shock compressive stress on the target plate. When the first fragment impacted the target plate, the pressure on the target plate was 2.033 MPa. More fragments in the central area then arrived at the front face of the target plate. The plate was hit violently, resulting in shear failure in the central area of the target plate, forming a plugging breach. For fragments outside the central area, the velocity along the normal direction of the target plate decreased, and the velocity in the horizontal direction increased. The destructive effect on the target plate decreased gradually, showing an embedding and ricocheting mode.

4.2.2 Dynamic response of PU coated on front face

The typical failure process of group F (F-4) is shown in Figure 18. The failure process can be divided into three stages.

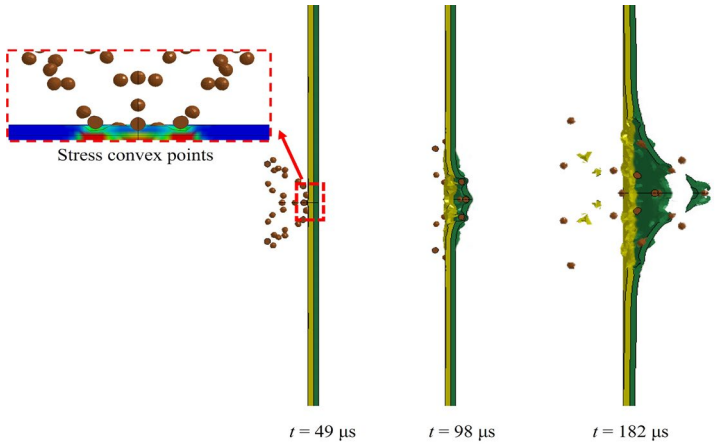

Figure 18 Process of shock-fragments loading on the target plate of F-4.

Stage 1. The shock wave reached the PU coating first, and the PU was sheared and torn in the central area and squeezed outward, resulting in the formation of a pit.

Stage 2. When the fragments arrived, the size of the pit further increased, resulting in large-area unit failure. Under the combined action, the plastic stress of the PU in the central penetration area increased. At the same time, the stress wave would propagate inside the target plate and had a destructive effect on the target plate. For polyurea-steel plate composite structure, there was an impedance mismatch effect due to the great difference between the wave impedance of the two materials (Han et al., 2020). When the stress wave propagated at the polyurea-steel plate interface, it was reflected and transmitted, resulting in stress concentration at the interface, as shown in Figure 18. In addition, AMMT-53 polyurea had the characteristics of high hardness and low elongation, the polyurea was degummed and broken seriously, resulting in a large cavity near the center of the target plate. A large number of perforations appeared on the outside of the central area. With the increase in the distance from the center of the target plate, the power of the fragments reduced. They were unable to penetrate the target plate and produced craters on the plate. At this stage, the steel plate deformed along the normal direction due to the energy transmitted from the PU layer.

Stage 3. In this stage, the failure processes of F-2, F-4, and F-6 were different due to the different thicknesses of the PU layer. Part of the kinetic energy of the fragments in F-2 had been consumed in stages 1 and 2, and the velocities of the fragments had been greatly reduced. When the first fragment impacted the target, it produced a pressure of 1.603 MPa on the steel plate. However, because the thickness of the PU layer was too thin, before the fragments penetrated the PU layer completely, the PU fragments caused by the combined action had begun to penetrate the steel plate and superimpose with the fragments that arrived later. This led to an uneven stress distribution on the steel plate, resulting in convex stress points, as shown in Figure 19. When the fragments broke through the PU layer, a more violent superposition effect was generated. The steel plate was subjected to shear failure, formed a break in the central area, and then tore along the penetration direction of the fragment. Finally, four 'petals' formed under the action of the shock wave pressure, resulting in petalling failure. When the first fragments of F-4 and F- 6 impacted the steel plate, pressures of 1.487 and 1.203 MPa were generated on the steel plate, respectively. A stress concentration area formed at the center of the steel plate. For F-4, the stress in this area exceeded the maximum tensile strength of the steel plate and produced shear failure. However, in F-6, the energy of the stress concentration area did not exceed the maximum tensile strength and only produced deformation in the normal direction. The development history of the central deformation of group F is shown in Figure 20.

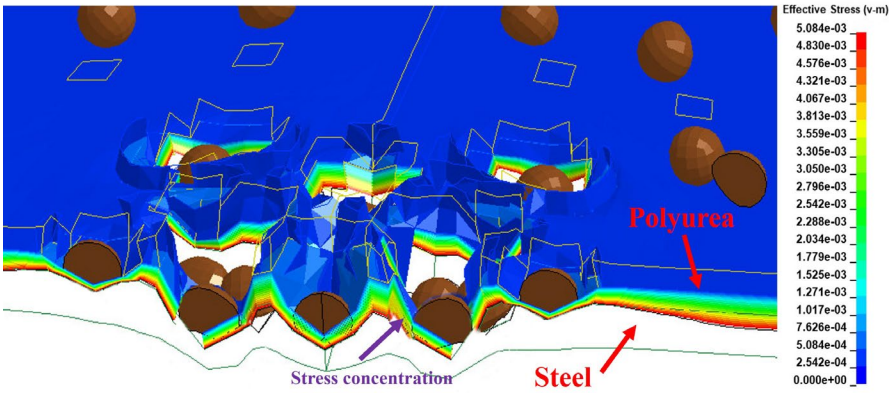

Figure 19 Concentration effect of stress at material interface.

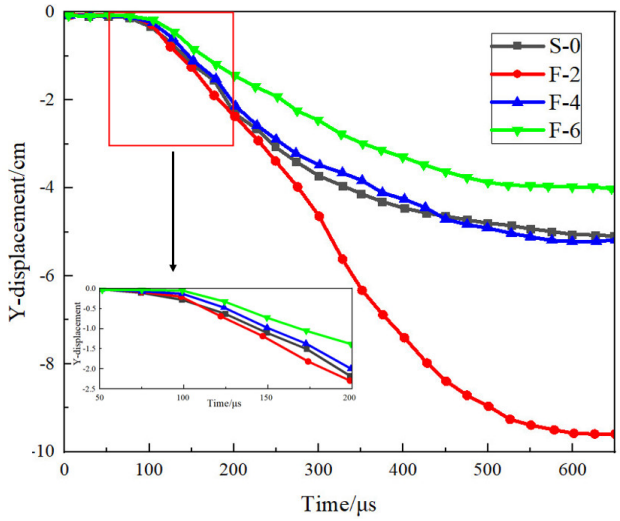

Figure 20 Center displacement histories of group F.

4.2.3 Dynamic response of PU coated on back face

The failure process of group B is shown in Figure 21, and it can be divided into two stages:

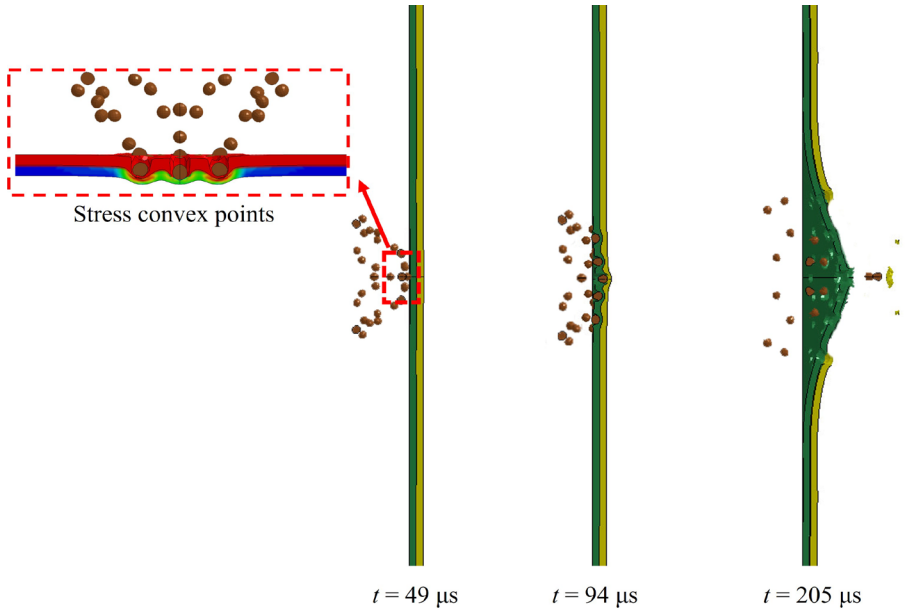

Figure 21 Process of shock-fragments loading on the target plate of group B-4.

Stage 1. This stage was similar to S-0.

Stage 2. When the stress wave was transmitted from the steel plate to the PU layer, the PU was subjected to tensile stress. Due to the strong adhesion with the steel plate, the PU layer produced plastic strain with the steel plate, absorbed the energy transmitted by the steel plate, and restricted the deformation of the steel plate. As the steel plate was broken down by fragments, the PU in the central area was subjected to stress concentration, resulting in an inconsistency between the strain rate of the PU and steel plate. This caused the polyurea to tear and peel off from the steel plate, forming flying fragments. It should be noted that the convex stress points shown in Figure 21 were generated on the PU layer before the steel plate was broken down, the stress was concentrated at these points. Resulting in the degumming of the PU at this point, which would reduce the protection ability of the area. In this structure, although only a few fragments could penetrate the target plate because the stress transmitted by the steel plate exceeded its maximum tensile strength, the PU in the whole action area was peeled off from the steel plate on a large scale and formed a large number of fragments that flew away. Figure 22 shows the displacement time history of the center point of group B.

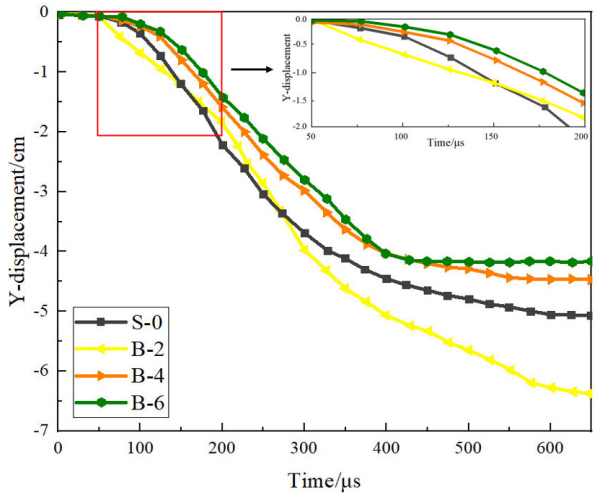

Figure 22 Center displacement histories of group B.

4.2.4 Dynamic response of PU coated on both faces

The failure process and deformation curve of group D are shown in Figures 23 and 24, respectively. The failure can be regarded as the combination of the failure processes of groups F and B, described as follows:

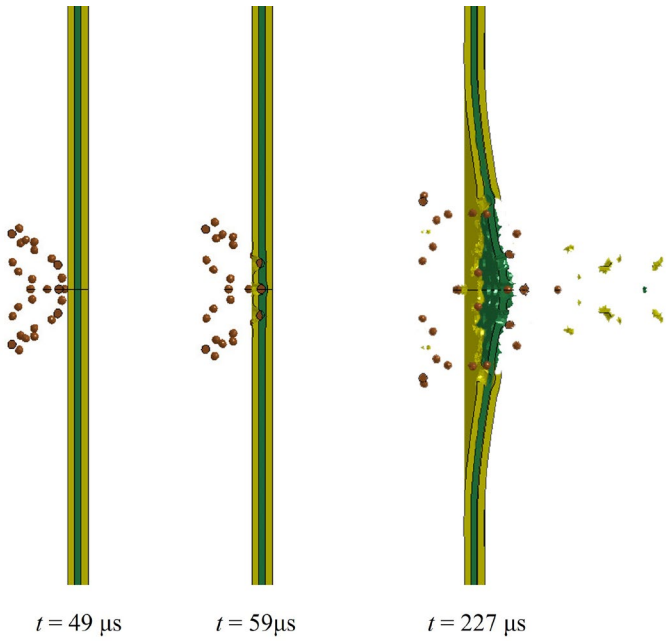

Figure 23 Process of shock-fragments loading on the target plate of group D-4.

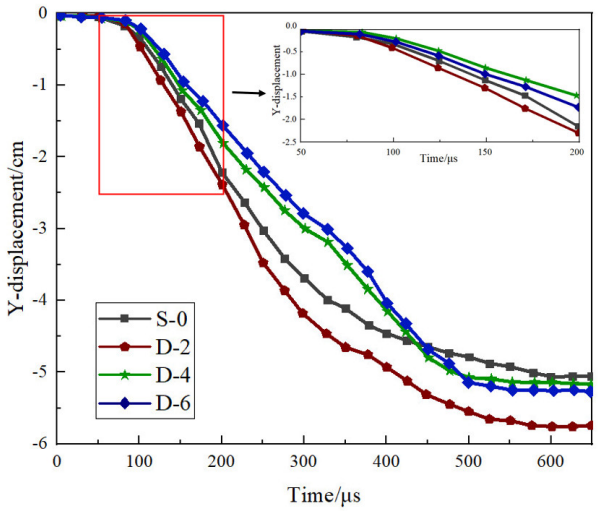

Figure 24 Center displacement histories of group D.

Stage 1. The failure mode and process of the front PU layer were similar to those in the first stage of group F.

Stage 2. The back PU layer played a restrictive role on the steel plate. Therefore, even if the steel plate was subjected to the stress transmitted from the front PU layer, it did not produce large bending and deformed before the front PU layer was penetrated completely.

Stage 3. As time progressed, the energy was transferred to the back PU layer, and the steel plate was further stretched, resulting in large deformation. When the energy exceeded the maximum tensile strength of the PU layer, the damage similar to that of group B occurred on the PU of the back face, and the PU in the central area was stripped away. However, the polyurea in the front and back face increased the overall stiffness of the target plate. It limited the steel plate to dissipate energy by plastic deformation, the excess stress was concentrated among the perforations, as shown in Figure 25, and finally, the target plate was torn along the perforations. Tearing cracks had an adverse effect on the integrity of the target plate, and the anti-deformation ability decreased sharply. Under the action of the residual impact energy, the target plate was further deformed. As a result, the final protective effect was not as good as that of the target coated with PU on a single side.

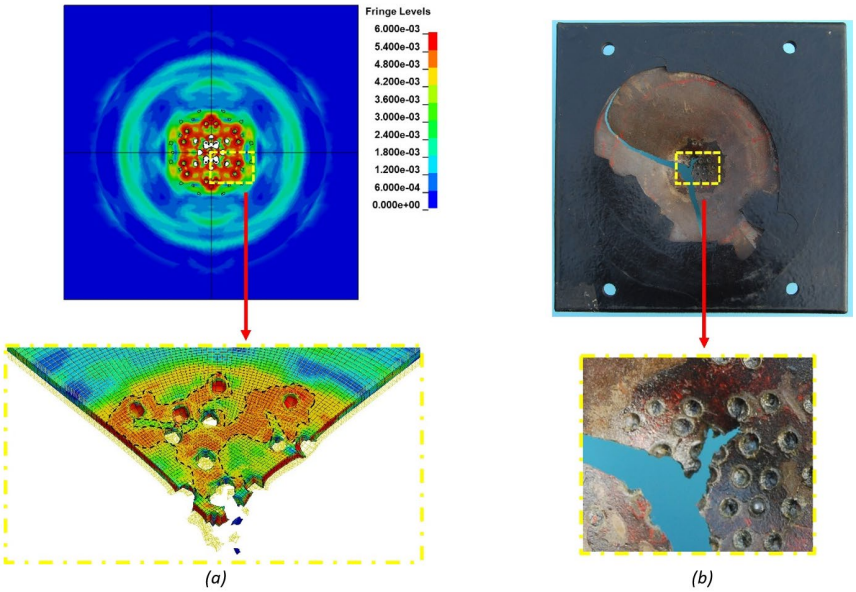

Figure 25 Von Mises stress concentration near the fragment perforations.

4.3 Impulse analysis of PCSPs

The blast shock wave and fragments impacted the target plate in the form of impulse and destroyed the target plate. After being impacted by the combined action, the process of impulse change on the target plates with different configurations was different.

Figure 26 shows the impulse time curve of the steel plate in the above four conditions. Among them, the measuring points in the central damaged area of F-4 and D-2 steel plates were deleted at 294 μs and 238 μs respectively, so the impulse time curves of these two conditions were incomplete. As can be seen from Figure 26, each curve had 2 peak points in the range of 28 μs-45 μs. The first peak point corresponded to the maximum impulse caused by the shock wave, and the second was the maximum impulse received by the steel plate when impacted by the central fragment. Subsequently, the curves decreased rapidly and showed a trend of choppy with the subsequent fragments impacting the target plate.

For S-0, the steel plate was directly impacted by the combined action, the peak impulse and the amplitude of the steel plate were the largest. For F-4, the PU coated on the front played a certain buffer role, reducing the impulse of the shock wave to the steel plate, but the impulse of the central fragment to the steel plate was increased slightly compared with S-0. Because the PU coated on the back played a supporting role on the steel plate, the impulse peak of B-4 was significantly reduced. The first peak point of D-2 was the smallest of all curves, but the second peak point was almost consistent with B-4.

Under the test and numerical simulation conditions in this manuscript, it can be inferred that PU coated on the back can effectively reduce the impact of shock wave and high-speed fragments on the steel plate. PU coated on the front can effectively absorb the impact of the shock wave, but it reduced the ability of the steel target to resist the impact of high-speed fragments. When PU was coated on double sides, it can be regarded as the combination of the above two situations.

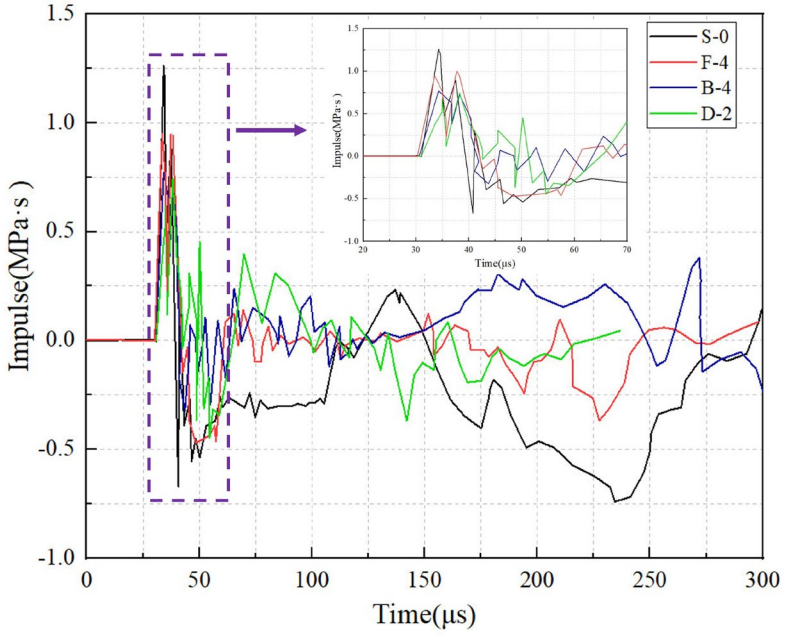

Figure 26 Time-history curves of impulse for steel plate in different conditions.

4.4 Energy absorption analysis of PCSPs

The analysis of the energy absorption of PCSPs is very important for explaining the combined protection effect. To explore the energy absorption effect of each structure, S-0, F-4, B-4, and D-2 were selected for analysis and comparison.

The energy change process of the PCSP is shown in Figure 27. Figure 27 (a) shows that the kinetic energy of each steel plate had a significant peak. The kinetic energy value fluctuated for a period near the peak point and then declined. This fluctuation process corresponded to the process of the steel plates being penetrated by fragments. The kinetic energy peak of S-0 was the largest, reaching 1.23 kJ at t = 107 μs. The kinetic energy peak of F-4 reached 1.11 kJ when t = 105 μs and that of B-4 reached 0.71 kJ at t = 87 μs. The smallest peak was for D-2, which reached a maximum of 0.65 kJ at t = 69 μs. The values of the kinetic energy peaks of F-4, B-4, and D-2 were 90.4%, 58.0%, and 52.3% of that of S-0, respectively.

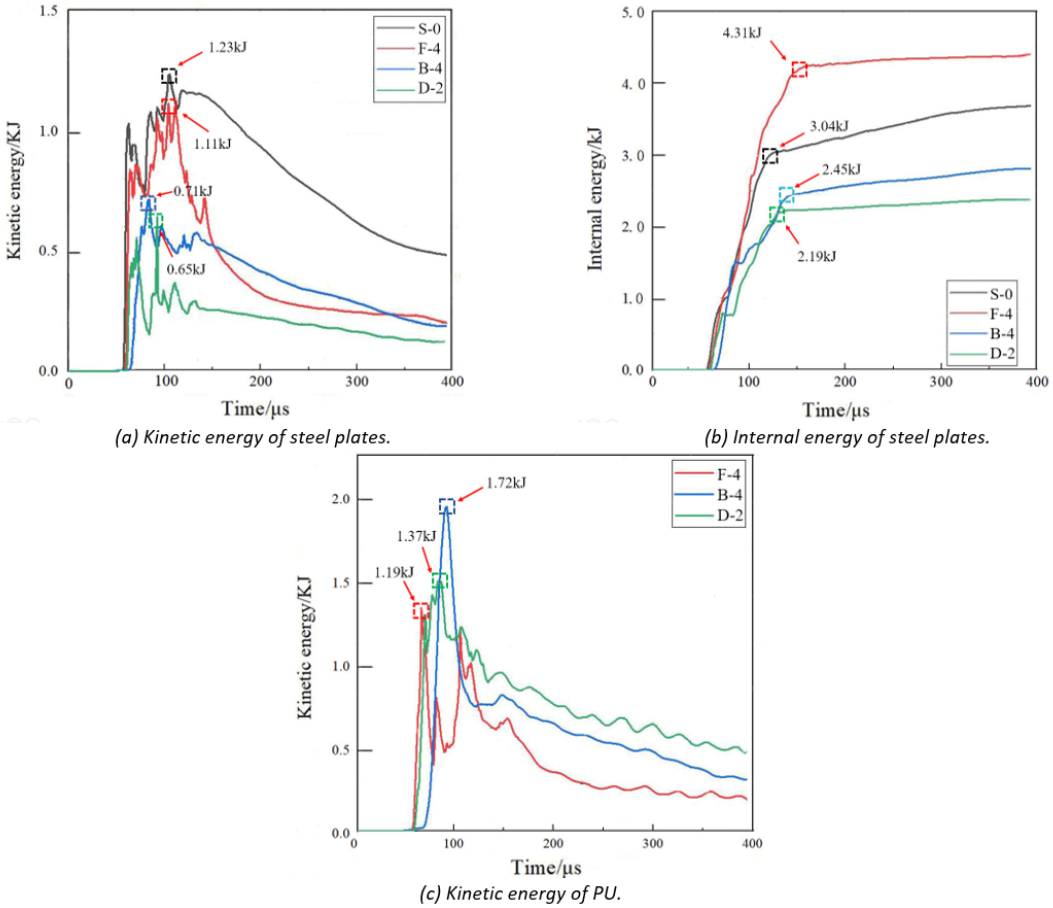

(a) Kinetic energy of steel plates.

(b) Internal energy of steel plates.

(c) Kinetic energy of PU.

Figure 27 Time-history curves of energy absorption for PCSPs.

Internal energy was generated in the steel plates. As shown in Figure 27 (b), the internal energy of the steel plates showed an upward trend during the whole process, and an inflection point was evident. The time of the inflection point roughly corresponded to the time when the kinetic energy of the steel plate began to decline after the vibration. The internal energies at the inflection points for the plates were in the following order: F-4 > S-0 > B-4 > D-2. S-0.

The variation process of the kinetic energy in PU with time is shown in Figure 27 (c). The maximum kinetic energy of PU in F-4, B-4, and D-2 were 1.19, 1.72, and 1.37 kJ, respectively, appearing at t = 62, 95, and 91 μs. This also corresponded to the failure degree of each PU layer. The PU coatings of the front faces in F-4 and D-2 were damaged directly by the combined action, which suffered the greatest impact compression and penetration effects, and the kinetic energy of the PU layers increased rapidly. However, due to the restraint of the lower plate, the kinetic energy peaks were not large. For B-4 and D-2, the PU of the back faces was not damaged by the combined action first. However, these layers were not constrained by the lower plate, and therefore, the kinetic energy increased slowly, but the peak values were high.

By the energy-time curves of PCSPs under different conditions, it can be found that the deformation deflection of D-2 was the largest, while the kinetic energy and internal energy of steel plate were the lowest. This was because the impact energy was not only dissipated to a certain extent through the polyurea coated on double sides, but the steel plate was seriously torn when it was impacted, and a large amount of impact energy was dissipated. This phenomenon is so called unloading explosion effect (Zhang, 2020). Similarly, although the final deformation deflection of F-4 was slightly higher than that of S-0, the kinetic energy of F-4 steel plate was slightly lower than that of S-0 because of the larger punching failure area and more internal energy accumulated in the steel plate of F-4. Due to a large amount of impact energy absorbed by PU, the damage degree of B-4 was the lightest, and the deformation deflection was the lowest. Therefore, it can be concluded that the polyurea coated on the front had the lowest energy absorption efficiency and it accumulated the impact energy on the steel plate. The polyurea coated on the back had the highest energy absorption efficiency, it consumed a lot of impact energy and reduced the damage degree of the steel plate. Although the energy absorption efficiency of polyurea coated on double sides was higher than that of polyurea coated on the front, the steel plate was seriously torn, thus greatly dissipating the impact energy of steel plate. In addition, the PU was degummed and cracked prematurely also limited the effect of energy absorption.

4.5 FTIR results and discussion

Regarding the energy absorption mechanism of PU, previous research results showed that PU consumes energy mainly through the glass transition of its internal structure after impact (Sarva et al., 2007; Bogoslovov et al., 2007). However, it was not possible to directly extract the data of glass transition of polyurea from FE simulations. The degree of glass transition of polyurea under high dynamic loading can be characterized by comparing the composition and number of specific chemical bonds in polyurea molecules (Li et al., 2016).

PU is a high molecular polymer whose physical properties are determined by its chemical composition. The microphase separation characteristics and hydrogen bond connecting soft and hard segments in PU are the keys to determine the high strain rate effect and energy absorption (Manav and Ortiz, 2021; Yao et al., 2020). The distribution of different chemical bonds in PU could be obtained by FTIR, which was helpful to further study the energy absorption mechanism of PU. Figure 28(a) is the results obtained after FTIR test of the above five samples. Each spectrum in Figure 28 was normalized according to the processing method of References (James et al., 2003). The results showed that the FTIR curves of PU coatings at different positions were roughly the same, but the corresponding oscillation amplitudes were significantly different.

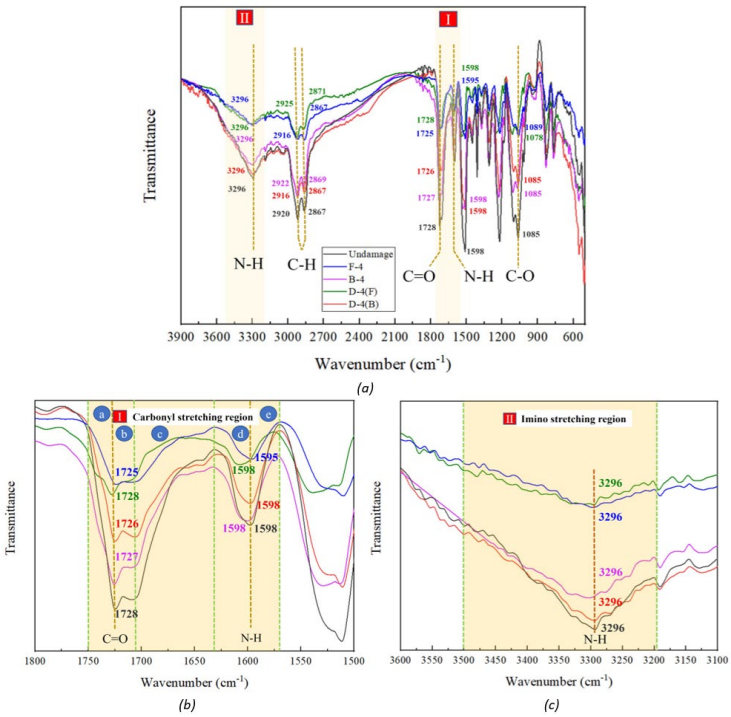

Figure 28 (a) The results of FTIR; (b) Carbonyl stretching region; (c) Imino stretching region.

For PU, two regions of FTIR spectrum were particularly important (James et al., 2003). The first was the carbonyl stretching region, which was located between 1565 $cm^{-1}$to 1750 cm^{-1} for this type of PU, and James T. divides it into five separate basebands (James et al., 2003), as shown in Figure 28(b). The absorption peak at 1725 cm^{-1} was the carbonyl group of hard segment and soft segment (C=O). The absorption peak at 1598 cm-1 represented the hydrogen bond connecting N–H and C=O.

The second important area was the imino stretching region between 3190 cm^{-1} and 3500 cm^{-1}. The occurrence of the absorption peak at the wavenumber of 3296 cm^{-1} in this region was related to the tensile vibration of the hard segment (Mccarthy et al., 1997; Hideaki et al., 1974). According to the test conducted by Li et al. (2016), the fracture of hydrogen bonds in this region was an important form of energy dissipation of PU in the tensile process. The absorption peaks with wavenumbers of 2916 cm^{-1} and 2867 cm^{-1} were attributed to the antisymmetric tensile vibration and symmetric Tensile vibration of the C-H bond of hard segment, respectively. In the spectral range of wavenumbers from 1500 cm^{-1} to 1730 cm^{-1}, the absorption peaks were the vibration of carbonyl (C=O) in hard and soft segments.

Based on the above theory, the relative degree of microphase separation can be evaluated by measuring the oscillation degree of C=O hydrogen bond in PU (Bummer and Knutson, 1990). The increase of microphase separation degree is accompanied by the increase of absorbance of ordered C=O peak (Luo et al., 1997). As can be seen from ta 28, after the PU coated on the back (B-4 and the back of D-4) was subjected to the tensile action of the combined action, the

area of the carbonyl stretching region and the imino stretching region was decreased and decreased of the peak area represented the hydrogen bond was broken and the microphase separation was damaged. In the process of fracture, the hydrogen bond dissipates energy. The carbonyl stretching region and the imino stretching region area of PU coated on the front (F-4 and the front of D-4) was greatly reduced. This was because, in addition to being directly damaged by combined action, it was also ablated by detonation products, which seriously destroyed the intramolecular structure and greatly reduced the protective performance, which was consistent with the SEM test results.

5. Conclusions

In this paper, the damage responses and protection mechanisms of PU-reinforced steel plates with different coating methods under the combined action of explosion shock waves and fragments were investigated through experiment, numerical simulations and microanalysis. The following conclusions were drawn.

(1) Under the experimental conditions in this paper, the shock wave reached the target plate before the fragments, and the target plate was first affected by the shock wave and then penetrated by the fragments. The combined action of the shock wave and the fragments was not just a simple superposition.

(2) Under the experimental conditions in this study, it was found that the improvement of the protective ability of the PU coated on the steel plate did not increase linearly with the thickness. PU coatings with thicknesses of more than 4 mm on one side could enhance the protective ability against the combined action. The thicker the coating, the higher the protection ability. When 6-mm-thick PU was coated on the front and back faces, the maximum damage deflection could be reduced by 20.8% and 18.5%, respectively. However, when the coating thickness was 2 mm, the damage degree would be aggravated, and the damage in the central area was manifested as petal failure. When PU was coated on both sides, the damage degree of the target plate could not be reduced, regardless of the thickness of PU.

(3) The protection principle of PU was explained from the perspective of the dynamic response, impulse change process and energy absorption. The PCSP with PU coating on the front face reduced the impulse of the shock wave to the steel plate, but the impulse of the central fragment to the steel plate was increased. The PU coated on the back effectively reduced the impact of shock wave and high-speed fragments on the steel plate, and the energy absorption efficiency was the strongest. The double-sided PU coating had common characteristics with the front and back coatings, but it limited the energy absorption of the steel plate to the form of large deformation, resulting in stress concentration at the perforation connections. This caused tearing cracks, and the integrity of the PCSP was sharply reduced.

(4) Through the microanalysis of PU samples by SEM and FTIR, it was concluded that the failure mechanisms of PU at different coating positions were different under combined action. The PU coated on the back mainly dissipated energy in the way of tensile fracture, while the PU coated on the front also suffers from the direct ablation of detonation products, the damage was more serious, and the failure mechanism was more complex. The breaking of hydrogen bond in PU molecule was the key to determining the energy absorption performance.

Acknowledgement

This research was supported by the National Natural Science Foundation of China (Grant Nos. 51978660 and 12102480). The authors would like to gratefully acknowledge this support.

Author's Contributions: Writing - original draft, L Zhang; **Test technical support,** C Ji, YT Wang and G Wu; **Writing - review & editing,** J Gu and LY Cheng; **Numerical simulation technical support,** X Wang.

Editor: Marcílio Alves

References

Wang H, Deng X, Wu H, Pi A, Li J, Huang F. (2019). Investigating the dynamic mechanical behaviors of polyurea through experimentation and modeling. Defence Technology 15(6):875-884.

Toutanji HA, Choi H, Wong D, Gilbert JA, Alldredge DJ. (2013). Applying a polyurea coating to high-performance organic cementitious materials. Construction & Building Materials 38(JAN):1170-1179.

Crouch I G. (2019). Body armour-new materials, new systems. Defence Technology 15(3): 241–253.

Stergiou T, Baxevanakis K P, Roy A, et al. (2021). Impact of polyurea-coated metallic targets: Computational framework. Composite Structures 113893.

Grujicic, M, BP D'Entremout, B Pandurangan, J Runt, J Tarter, G Dillon. (2012). Concept-Level Analysis and Design of Polyurea for Enhanced Blast-Mitigation Performance. Journal of Materials Engineering & Performance 21(10):2024-2037.

Jacobs M. J. N., Van Dingenen J. L. J. (2001). Ballistic Protection Mechanisms in Personal Armour. Journal of Materials Science 36(13):3137-3142.

Jena P. K., Mishra B., Ramesh-Babu M., Babu A., Singh A. K., SivaKumar K., Bhat T. B. (2010). Effect of heat treatment on mechanical and ballistic properties of a high strength armour steel. International Journal of Impact Engineering 37(3):242–249.

Ackland K, Anderson C, Ngo TD. (2013). Deformation of polyurea-coated steel plates under localised blast loading. International Journal of Impact Engineering 51(JAN):13-22.

Nemat-Nasser M. (2010). Investigation of effect of polyurea on response of steel plates to impulsive loads in direct pressure-pulse experiments. Mechanics of Materials 42(6):628-639.

Amini MR, Amirkbizi AV, Nemat-Nasser S. (2010). Numerical modeling of response monolithic and bilayer plates to impulsive loads, International Journal of Impact Engineering (1); 30:90–102.

Zeng L, Liang H, Liu L, Zhang Q. (2021). Anti-explosion Design Method for Aluminum Alloy Doors in Ordinary Buildings. Journal of Failure Analysis and Prevention 21(1):268-279.

Mohotti D, Ngo T, Raman SN, Mendis P. (2015). Analytical and numerical investigation of polyurea layered aluminum plates subjected to high velocity projectile impact. Materials & design 82(5):1-17.

Mohotti D, Tuan, Ngo, Sudharshan, N., et al. (2014). Plastic deformation of polyurea coated composite aluminum plates subjected to low velocity impact-ScienceDirect. Materials & design 56:696-713.

Huang X, Zhang W, Deng Y, Jiang X. (2018). Experimental investigation on the ballistic resistance of polymer-aluminum laminated plates. International Journal of Impact Engineering 113:212-21.

Dinesh, R., P. Vasundra, D. D. Jebaseelan. (2021). A Finite Element Analysis Based Study on Effects of Polyurea Coating for Blast Mitigation. IOP Conference Series Materials Science and Engineering 1128(1):012046.

Wu G, Wang X, Ji C, Gao Z, Liu Y. (2021a). Anti-blast properties of 6063-T5 aluminum alloy circular tubes coated with polyurea elastomer: Experiments and numerical simulations. Thin-Walled Structures 164(7): 107842

Dewapriya M, Miller RE. (2021). Energy absorption mechanisms of nanoscopic multilayer structures under ballistic impact loading. Computational Materials Science 195(34):110504.

Sun YX, Wang X, Ji C, Zhao CX, Jiang T. (2021). Experimental Investigation on Anti-penetration Performance of Polyurea Coated ASTM1045 Steel Plate Subjected to Projectile Impact. Defence Technology 17(4): 1496-1513.

Chepkenen, P, Ochieng D, Wando A. O. (2020). Mitigation Measures on Improvised Explosive Device (IED) Attacks in Mandera East Sub County, Mandera County, Kenya. International Journal of Science and Research 9(8):1071-1078.

Kong X S, Wu W G, Li J, Liu F. (2014). Experimental and numerical investigation on a multi-layer protective structure under the synergistic effect of blast and fragment loadings. International Journal of Impact Engineering 65:146-162.

Nyström U, Gylltoft K. (2009). Numerical studies of the combined effects of blast and fragment loading. International Journal of Impact Engineering 36(8):995-1005.

Duan, X, Cheng Y, Zhang P, Liu J, Yang L. (2015). Numerical analysis of the damage on I-core sandwich panels subjected to combined blast and fragment loading. Chinese Journal of Ship Research 10(6):45-59.

Leppaenen J. (2005). Experiments and numerical analyses of blast and fragment impacts on concrete. International Journal of Impact Engineering 31(7):843-860.

Molnar W, Nugent S, Lindroos M, Apostol M, Varga M. (2015). Ballistic and numerical simulation of impacting goods on conveyor belt rubber. Polymer Testing 42:1–7.

Wu G, Wang X, Ji C, et al. (2021b). Experimental and numerical simulation study on polyurea-coated fuel tank subjected to combined action of blast shock waves and fragments. Thin-walled structures 169:108436.

Xu R Q, Cui Y P, Z R. (2008). Study on shock wave attenuation characteristics in plexiglass. Laser technology 3: 3-5+ 21. (in Chinese).

Nan YX, Jiang JW, Wang SY, Fang YJ. (2013). Numerical simulation and test for impact response of submunitions drop. Vibration and shock 32(3):182-187. (in Chinese).

Johnson GR, Cook WH. (1983). A constitutive model and data for metal subjected to large strains, high strain rates and high temperature. Engineering Fracture Mechanics 21:541-548.

Lundberg P, Renstroem R, Lundberg B. (2006). Impact of conical tungsten projectiles on flat silicon carbide targets: Transition from interface defeat to penetration. International Journal of Impact Engineering 32(11):1842-1856.

Wang JG. (2017). Dynamic load Resistance of clay brick masonry reinforced by spraying polyurea. Hefei. University of Science and Technology of China. (in Chinese).

Raman SN, Ngo T, Mendis P, et al. (2012). Elastomeric polymers for retrofitting of reinforced concrete structures against the explosive effects of blast. Adv Material Science Engineering 2012:1–8.

Shi SQ, Liao Y, Peng XQ, et al. (2019). Behavior of polyurea-woven glass fiber mesh composite reinforced RC slabs under contact explosion. International Journal of Impact Engineering 132(OCT.):103335.

Raman SN, Ngo T, Lu J, et al. (2013). Experimental investigation on the tensile behavior of polyurea at high strain rates. Material & Design 50:124–9.

Zheng HW, Chen CH, Li M. (2019). Simulation analysis of flow around fragments with different Shape by air blasting shock wave. Ship Science and Technology 41(9):31-36. (in Chinese).

Han ZY, Li DY, Zhou T, et al. (2020). Experimental study of stress wave propagation and energy characteristics across rock specimens containing cemented mortar joint with various thicknesses. International Journal of Rock Mechanics and Mining Sciences 131:104352.

Zhang P. (2020). Study on Anti-Ballistic and anti-explosion protection performance and mechanism of polyurea coated structure. Taiyuan. Zhongbei University. (in Chinese).

Sarva S S, Deschanel S, Boyce M C, et al. (2007). Stress-strain behavior of a polyurea and a polyurethane from low to high strain rates. Polymer 48(6):2208-2213.

Bogoslovov R B, Rolad C M, Gamache R M. (2007). Impact induced glass transition in elastomeric coatings. Applied Physics Letters 90(22):2219-2223.

Li T, Dai Z, Xie Z, et al. (2016). Study on hydrogen bond behavior of polyurea during stretching. National symposium on polymer materials science and engineering of China. (in Chinese).

Manav M, Ortiz M. (2021). Molecular dynamics study of the shock response of polyurea. Polymer 212:123109.

Yao K, Liu Z, Li T, et al. (2020). Mesoscale structure-based investigation of polyurea dynamic modulus and shock-wave dissipation. Polymer 202(5):122741.

James T Garrett, Xu R, Cho J, et al. (2003). Phase separation of diamine chain-extended poly(urethane) copolymers: FTIR spectroscopy and phase transitions. Polymer 44:2711-2719.

Mccarthy S J, Meijs G F, Mitchell N, et al. (1997). In-vivo degradation of polyurethanes: transmission-FTIR microscopic characterization of polyurethanes sectioned by cryomicrotomy. Biomaterials 18(21):1387-1409.

Hideaki, Ishihara, Itsuro, et al. (1974). Infrared studies on segmented polyurethane-urea elastomers. Journal of Macromolecular Science Part B.

Bummer P M, Knutson K. (1990). Infrared spectroscopic examination of the surfaces of hydrated copoly(ether-urethane-ureas). Macromolecules 23(20):4357-4362.

Luo Y, Wang DN, Ying SK. (1997). Hydrogen-Bonding Properties of Segmented Polyether Poly (urethane urea) Copolymer. Macromolecules 30(15):4405-4409.